

Enabling pulse shape discrimination with commercial ASICs

John Leland^a, Ming Fang^a, Satwik Pani^{a,b}, Yuri Venturini^c, Marco Locatelli^c,
Angela Di Fulvio^{a,*}

^a*Department of Nuclear, Plasma, and Radiological Engineering, University of Illinois,
Urbana-Champaign, 104 South Wright Street, Urbana, IL 61801, United States*

^b*Department of Radiation Oncology, Washington University School of Medicine, 660 S.
Euclid Ave, St. Louis, MO, 63110 USA*

^c*CAEN Technologies Inc., 1 Edgewater Street - Suite 101 Staten Island, NY 10305, United
States*

Abstract

Fast electronic readout for high-channel density scintillator-based systems is needed for radiation tracking and imaging in a wide range of applications, including nuclear physics, nuclear security and nonproliferation. Programmable electronics, like FPGAs and ASICs, provide a fast way of conditioning and processing the signal in real time. In this paper, we present a pulse shape discrimination (PSD) method based on the shaping circuit of a commercially available ASIC, the Citiroc1A by CAEN Technologies. We used two different shaping times per detector channel to calculate a shaping parameter that enables PSD. Using our new method, neutron and gamma-ray pulses detected by a d₁₂-stilbene scintillator can be effectively discriminated at light output values greater than 0.15 MeVee. While not achieving the PSD performance of traditional offline charge integration, our method does not require the transfer of data to a separate system for further processing and enables the direct deployment of high-channel density multi-particle detection systems. Moreover, the availability of a wider range of shaping times than those on the Citiroc1A can potentially further improve the PSD performance.

Keywords: silicon photomultiplier, pulse shape discrimination, application specific integrated circuit

1. Background and Motivation

The availability of solid-state light readout devices, like silicon photomultipliers (SiPMs), makes it possible to scale large arrays of scintillation detectors [1, 2]

*Corresponding author. Tel.: +1 217 300 3769.

Email address: difulvio@illinois.edu (Angela Di Fulvio)

to hand-held versions [3, 4]. Compared to avalanche photo-detectors and photo-diodes, SiPMs exhibit better performances, e.g., higher gain, lower noise, and a faster response [5]. When SiPMs are coupled with pulse-shape discrimination (PSD) capable scintillators, they allow for the simultaneous detection of different types of radiation, e.g., gamma rays and neutrons. Furthermore, the advantage of using SiPMs is the ability to handle a high number of channels, in the order of hundreds, while maintaining a compact form factor, ideal for hand-held stand-off gamma ray and neutron imaging. Programmable electronics, like field programmable gate arrays (FPGA) and application specific integrated circuits (ASICs), are particularly suitable for the readout of SiPMs coupled to arrays of scintillation detectors because they can perform similar complex functions as traditional analog electronics [6] and fast digitizers [7] while being compact and featuring a high number of channels. However, implementing specific functions, such as PSD, requires the design of custom ASIC-based devices, which are cost prohibitive for small-scale projects.

In this work, we address this issue by developing a method to perform PSD using the commercially available Citiroc1A ASIC controlled by the A55CIT4-DT5550W readout system [8, 9] by CAEN Technologies (Viareggio, Italy). This PSD method does not require sampling and storing hundreds of samples for each detected pulse, which corresponds to the analog-to-digital conversion process implemented on fast digitizers. Additionally, our method can be performed on-board without the need of transferring the data to another device for analysis.

The ASIC-based method implements an architecture that extracts a pulse-shape-dependent parameter, which enables the discrimination of gamma-ray and neutron pulses. In the 70s, similar analog PSD methods were explored and implemented. These methods typically perform PSD using a shaping stage followed by a time-to-amplitude circuit and comparator that discriminates between neutron and gamma-ray pulses [10] [11]. While being inspired by the analog implementation, our method expands on the prior work by translating the analog architectures to digital processing and enables PSD for high-channel density detector arrays using advanced on-board signal processing. Therefore, the method we propose grants the capability to perform PSD on a compact detection system with a high number of channels for a broad range of applications, including nonproliferation, nuclear physics, and radiation protection.

We developed and implemented an on-board PSD method for the commercially available Citiroc1A ASIC [12]. In Section 2, we introduce the ASIC-based method, which we will call Digital Shaper (DS) PSD, to discriminate between neutron and gamma-ray pulses and calculate the circuit response function for optimizing the PSD parameter using template pulses. In Section 3, we apply the optimized PSD method on measured gamma-ray and neutron pulses. A comparison between the traditional charge-integration (CI) PSD and DS PSD is given. The discussion and conclusions are presented in Section 4

2. Methods

In this section, we describe the implementation of PSD using electronics available in the Citiroc1A ASIC. The DS PSD method will be demonstrated on synthetic pulses and experimentally measured data, and its performance will be compared with the traditional PSD method.

2.1. Imaging System Design

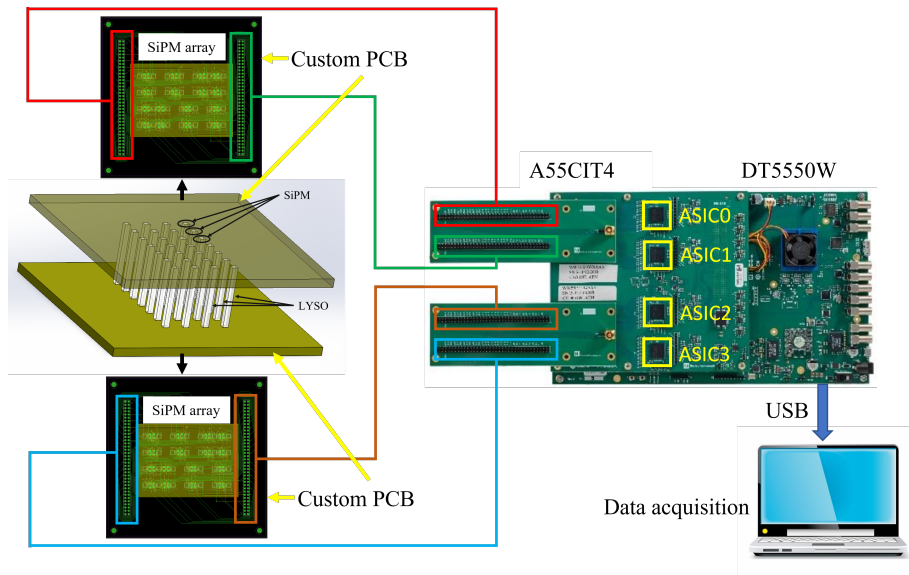


Figure 1: Schematic of a multi-particle spectroscopic imager based on an ASIC-based electronic readout.

We built a compact imaging system encompassing a 4×7 array of LYSO crystals ($3 \text{ mm} \times 3 \text{ mm} \times 5 \text{ cm}$) coupled to 56 Onsemi MicroFJ 30020 SiPMs [13] that are read out by four Citiroc1A ASICs. In the future the LYSO will be replaced by PSD-capable scintillators such as stilbene. This detector can be used as an imager for nuclear security and non-proliferation applications or as a particle tracker for nuclear physics experiments. Figure 1 shows the schematic of the imager. The system includes two custom printed circuit boards (PCBs), each powering and controlling the readout of a 4×7 array of SiPMs. The SiPM arrays are used for light readout of the top and bottom sides of a 4×7 scintillator matrix. The dual-end readout enables the retrieval of depth of interaction information [14, 15]. The SiPM pulses are fed to an A55CIT4-DT5550W readout system by CAEN Technologies [9]. The system is controlled via computer using the DT5550W Readout Software (Sci Digitizer Family, Version 2022.1.1.0, distributed by CAEN Technologies). This software allows us to control the DT5550W and program some of the board settings, including the gain, the

threshold, and the shaping constants. The A55CIT4 board hosts four Citiroc1A ASICs, each with a 32 readout channel capacity [8]. Thus, there are 128 input channels available in total. This board is particularly suitable for SiPM readout because it provides a bias from 20 V to 85 V with a current up to 10 mA [16]. In the current configuration, the board is set to provide a 30 V bias to the SiPMs. The A55CIT4 board features a fine time resolution better than 100 ps as stated by the manufacturer [8] and a 14-bit ADC with a sensitivity of 160 fC. We tested the effect of the Citiroc1A’s dead time on our data throughput using the DT5810B pulse generator. We found no loss of data when up to a 10 kHz input frequency. This acquisition rate is compatible with the detection of an approximately 6 mCi source at a distance of 1 m with our imager without. Therefore, the proposed configuration is suitable for imaging applications, even when measuring relatively high-intensity sources.

2.2. PSD Method

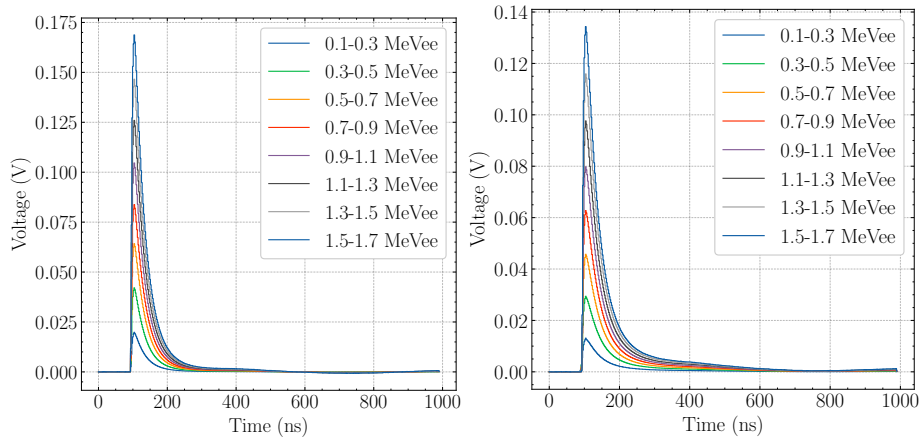
In this section, we briefly summarize the principles of two PSD methods, namely the traditional charge-integration PSD and the proposed DS PSD. The datasets used for the evaluation of the PSD methodologies are:

- A. Synthetic dataset acquired using a pulse generator connected to the ASIC
- B. Measured dataset produced using the SiPM evaluation board, digitizer, and stilbene-d₁₂
- C. Measured dataset produced using SiPM evaluation board, ASIC, and stilbene-d₁₂

2.2.1. Charge-integration PSD

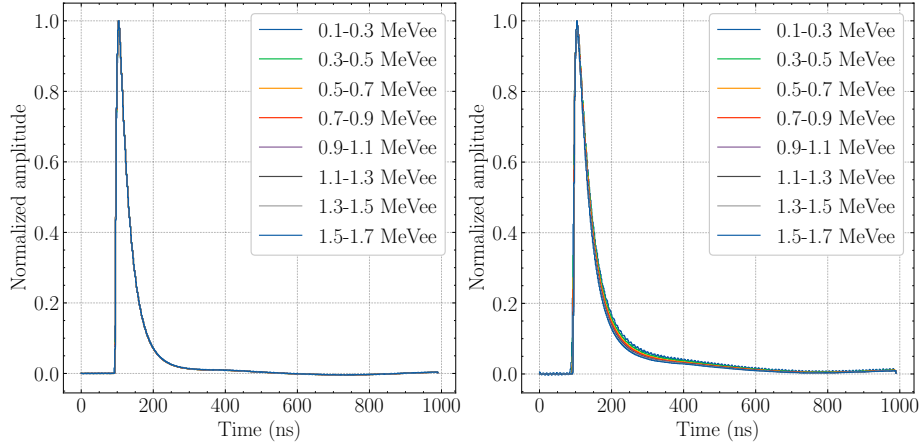
PSD-capable scintillators emit blue-UV light upon interaction with ionizing radiation through prompt and delayed fluorescence [17]. In organic scintillators, the light-emitting molecular excitation reactions are mainly due to recoil protons and electrons, produced by neutron and gamma-ray collisions, respectively. For an equivalent deposited energy, recoil protons produce a higher amount of delayed fluorescence, compared to electrons, due to their higher ionization density, which results in a larger delayed component in the detected pulses [17, 18]. This difference in delayed components can then be used to discriminate between gamma-ray and neutron pulses. Examples of template neutron and gamma-ray pulses are shown in Figure 2e, in which the neutron pulse shows a larger delayed component. The template pulses were obtained by binning the measured pulses in 0.2 MeVee-wide bins from 0.1 MeVee to 1.7 MeVee shown by Figures 2a and 2b, normalizing the gamma-ray and neutron pulses to their maximum values shown by Figures 2c and 2d and then averaging them in each bin separately shown by Figure 2e. The method used to obtain these pulses is described in further detail in Section 2.4.

Traditionally, charge integration (CI)-based PSD [19] is used to perform this discrimination. CI takes advantage of the difference in delayed components by defining the PSD parameter as the ratio of the area under the pulse tail to the



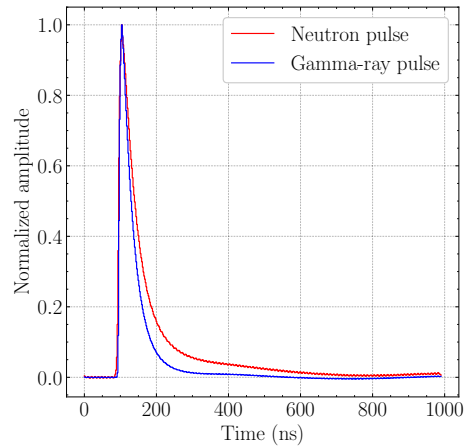
(a) Average gamma-ray pulses.

(b) Average neutron pulses.



(c) Normalized average gamma-ray pulses.

(d) Normalized average neutron pulses.



(e) Templates created by averaging pulses in entire light output range.

Figure 2: Normalized neutron and gamma-ray template pulses acquired by measuring a $^{239}\text{PuBe}$ source with a stilbene- d_{12} crystal. 5

total area (tail-to-total ratio) of the measured pulse, as shown by Equation (1). The pulses are measured in voltages as designated by $V(t)$ and t_0 is the beginning of the pulse, t_1 is on the falling edge of the pulse, and t_2 is the end of the pulse.

$$\text{PSD}_{\text{CI}} = \frac{\sum_{t_1}^{t_2} V(t)}{\sum_{t_0}^{t_2} V(t)} \quad (1)$$

Neutron pulses exhibit higher tail-to-total ratios due to the larger delayed components, which enables their discrimination from gamma-ray pulses.

2.2.2. Digital Shaper PSD

The Citiroc1A front-end encompasses a readout circuit with two independent paths, referred to as the low-gain (LG) and high-gain (HG) path. Each path consists of a low-gain/high-gain charge preamplifier, a pulse shaper, and a peak sensing circuit that detects and records the maximum of the shaped signal [8], as shown in Figure 3. Since gamma rays and neutrons have different pulse shapes, they exhibit different responses to the shaper in the Citiroc1A. It is therefore possible to perform PSD based on this difference in the shaper's responses.

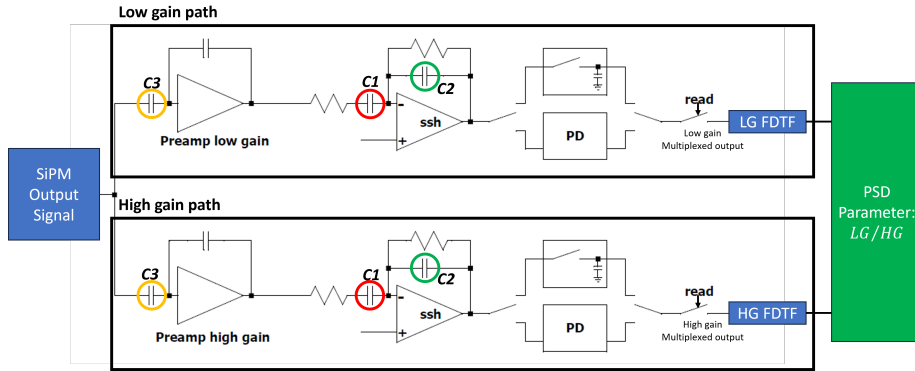


Figure 3: Calculation of the PSD parameter based on LG and HG outputs. SSH is the slow shaper and PD is the Peak Detector circuit [8].

For this method, the PSD parameter is defined as the ratio between the HG and LG output signals as shown by Equation (2). Due to the two paths of the readout circuit being linear with energy, the PSD parameter is mainly a function of the pulse shape with a slight dependence on the pulse height [20]. Figure 3 illustrates the steps needed to calculate the PSD parameter. The pulse shaper is shown in Figure 4. Its response is dependent on a set of three adjustable capacitances - C_1 , C_2 , C_3 - also shown in Figure 3. These capacitances are controlled through the “peak time” setting in the readout software. There are a total of seven available peak times each associated with a specific set of capacitances. To achieve the best PSD performance, we optimized the values of C_1 , C_2 , and C_3 to maximize the difference in PSD parameters of neutron and

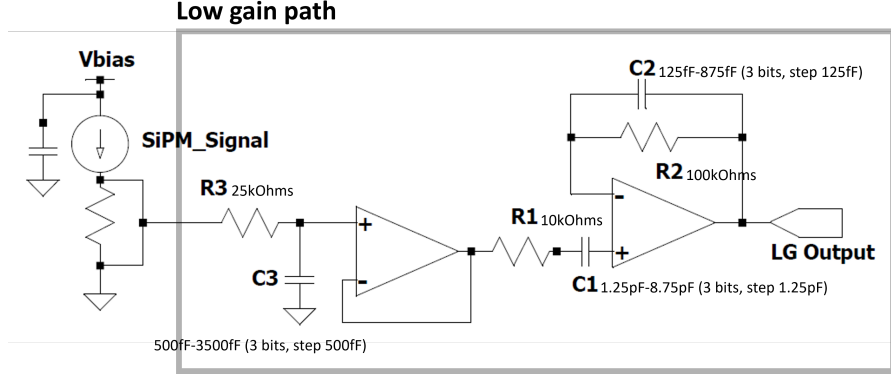


Figure 4: Single channel pulse shaper on the Citiroc1A. C1, C2, and C3 are the capacitances controlled by the peak time [12]

gamma-ray pulses. A detailed description of the optimization method is in the following Section 2.3.1.

$$\text{PSD}_{\text{ASIC}} = \frac{\text{HG output}}{\text{LG output}} \quad (2)$$

2.3. Computational Implementation of DS PSD

In this section, we calculate the response of the ASIC's acquisition chain, based on which we can determine the optimal ASIC settings for PSD.

2.3.1. Transfer Function and Pulse Shape

The response of the front-end acquisition chain of the ASIC was calculated based on the known architecture. A set of template gamma-ray and neutron pulses, shown in Figure 2, were used to test the response of the front-end to prototypical pulses. The template neutron and gamma-ray pulses were obtained by averaging 10,000 neutron and gamma-ray pulses, respectively, and normalizing them to the single pulse maximum value. The method used to obtain these pulses is described in Section 2.4 in greater detail.

We calculated the frequency-dependent-transfer-function (FDTF) of the pulse shaper (Figure 4) in the Laplace domain, shown by Equation (3). f stands for the frequency and $T(s)$ is the ratio between the output signal and input signal. C_1 , C_2 , and C_3 are the capacitances controlled by the peak time setting in peak sense mode of the readout software and the set relationship between the peak times and capacitances is shown in Table 1. The capacitances and R_1 , R_2 , and R_3 are shown in Figure 4 as well. The resistive values are specific to the ASIC itself and cannot be tuned by the user via software.

$$T(s) = \left(\frac{1}{sR_3C_3 + 1} \right) \left(\frac{s^2R_1C_1R_2C_2 + s(R_1C_1 + R_2C_2 + R_2C_1) + 1}{s^2R_1C_1R_2C_2 + s(R_1C_1 + R_2C_2) + 1} \right) \quad (3)$$

$$s = i\omega, \omega = 2\pi f$$

Table 1: Table of capacitances corresponding to the set peak time.

Peak Time (ns)	C_1 (pF)	C_2 (pF)	C_3 (pF)
87.5	1.25	125	500
75	2.50	250	1000
62.5	3.75	375	1500
50	5.00	500	2000
37.5	6.25	625	2500
25	7.50	750	3000
12.5	8.75	875	3500

We used the normalized template gamma-ray pulses in Figure 2e as the input to the FDTF to determine how the “peak time” affects the shape of the output signal. Figure 5 shows the unnormalized shape of the output signal at different peak times. As expected, a longer peak time corresponds to an increased delay of the peak timestamp of the shaped pulse.

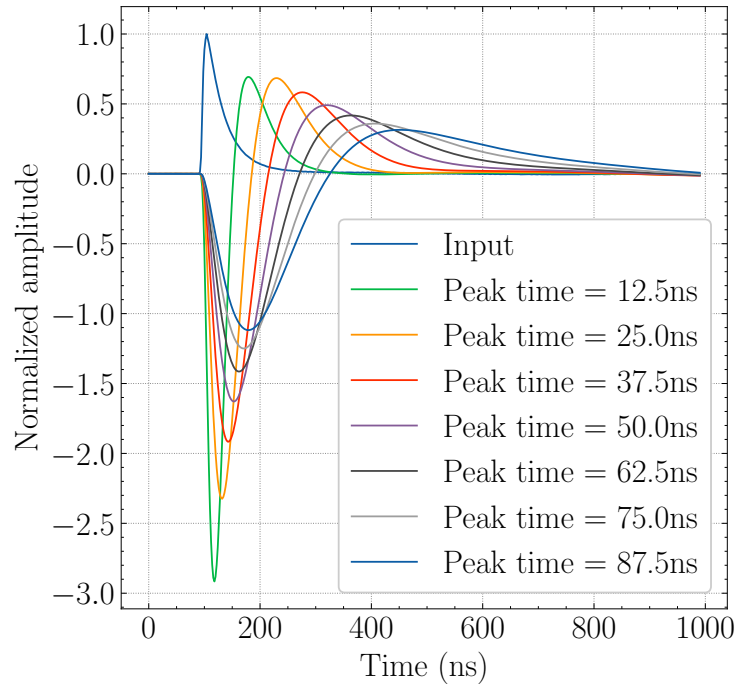


Figure 5: Signals output by FDTF with different peak times.

2.3.2. FDTF Optimization

The user can set the seven peak time values independently for the LG and HG paths, corresponding to 49 different combinations. For every combination

of LG and HG peak times, we feed a template pulse to the LG and HG transfer functions, calculate the LG and HG peak heights, and finally calculate the PSD parameter, which is the ratio between the HG and LG output signals. This procedure is performed for both gamma-ray and neutron template pulses. The combination of peak times that yields the largest difference between the gamma ray and neutron PSD parameters is optimal for discriminating the two types of pulses and was hence selected in this study.

2.4. Experimental Methods

With the optimized PSD settings, i.e., peak times, the DS PSD method is tested using two different data sets, one from a pulse generator and the other from measured data. The pulse generator was used to explore a broader range of pulse shapes and the measured data was used to determine the performance of the DS PSD.

2.4.1. Data Sets Used to Test the PSD performance

The emulated pulses were generated using the experimental setup in Figure 6. A DT5810B pulse generator [21] was directly connected to the A55CIT4 board. A laptop was connected to the A55CIT4 ASIC to program the board and acquired and visualize the PSD processed data. The pulse generator created exponential pulses with a pulse shape defined by Equation (4), where τ is the decay constant and OFFSET is 100 ns.

$$A \times \begin{cases} e^{-\frac{(t-\text{OFFSET})}{\tau}} & t \geq \text{OFFSET} \\ 0 & \text{otherwise} \end{cases} \quad (4)$$

Five decay constants were tested and the pulse height was uniformly distributed between 0 and approximately 0.3V. The shapes of the emulated pulses are shown in Figure 7.

The experimentally measured data set was obtained using a $3 \times 3 \times 5\text{mm}^3$ deuterated stilbene (stilbene-d₁₂) crystal coupled to a SenSL MicroFJ-30020 SiPM [13]. We set the over-voltage of MicroFJ-30020 SiPM to 2 V and the max signal amplitude was 0.2 V. The signal amplitude was low enough so that no severe signal saturation occurred in the HG channel, and high enough so that we could still acquire low-amplitude signals in the low light output range. The setup of DS PSD is shown in Figure 8. The SiPM signal is processed by the A55CIT4 board. A 1-mCi ²³⁹PuBe source was placed at a 10-cm distance from the deuterated stilbene crystal and measured for 30 minutes, resulting in approximately 200,000 pulses. For comparison, we replaced the A55CIT4 board with a 14-bit 500-MSps DT5730 digitizer and performed CI PSD on the saved pulses. The data set acquired with the digitizer was also used for the optimization of peak times described in Section 2.3. Examples of measured pulses are shown in Figure 2.

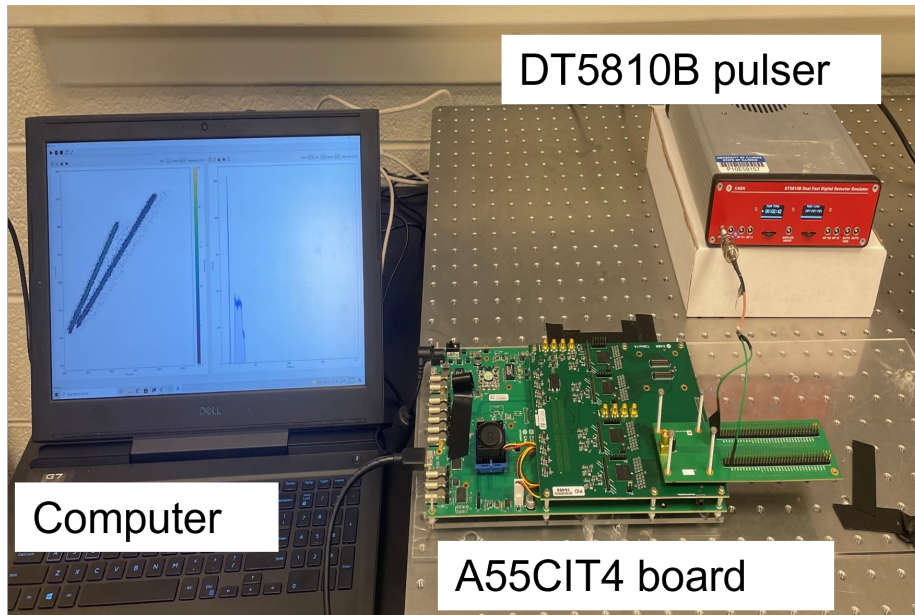


Figure 6: Emulated pulses experimental setup. The pulse generator output is connected directly to the ASIC and the output is recorded and processed in real-time by the computer to perform PSD.

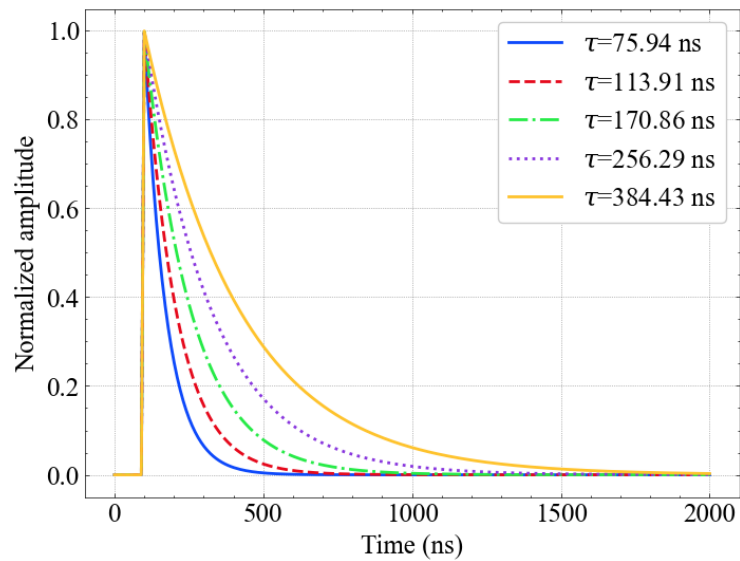


Figure 7: Normalized measured emulator pulses.

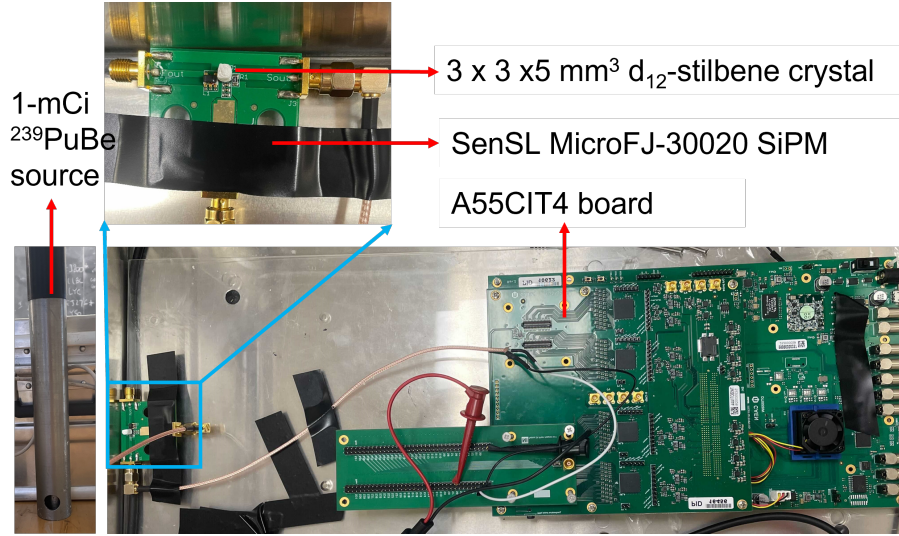


Figure 8: Measured data experimental setup. The SiPM output is sent to the ASIC and the signal is recorded by a computer.

2.4.2. Data Processing and Figure-of-Merit

PSD is performed on the emulated data and experimentally measured data using both the traditional charge integration method and the new PSD algorithm explained in the Section 2.2. The CI parameters for the total integral and tail-to-total integral are 300 ns starting 50 ns before the trigger and 220 ns starting 30 ns after the trigger, respectively. The results of the DS PSD are then compared with the results of the charge integration PSD. This comparison includes the PSD plots for a qualitative comparison and the calculated figure of merit (FOM) for a quantitative comparison. The FOM is calculated by performing a double Gaussian fit of the distribution of PSD parameters using Equation (5) and then using the parameters of the Gaussian fit as inputs to the FOM equation (Equation (6)) [22]. μ is the mean of one peak and $\text{FWHM}=2\sqrt{2\ln 2}\sigma$ is the full-width half-maximum of the same peak. A higher FOM is preferable because it corresponds to a wider separation between the neutron and gamma ray pulses in the PSD-parameter space.

$$f(x) = a_n \exp\left(-\frac{(x - \mu_n)^2}{2\sigma_n^2}\right) + a_\gamma \exp\left(-\frac{(x - \mu_\gamma)^2}{2\sigma_\gamma^2}\right) \quad (5)$$

$$\text{FOM} = \frac{|\mu_n - \mu_\gamma|}{\text{FWHM}_n + \text{FWHM}_\gamma} \quad (6)$$

3. Results

In this section we present the results of the optimization of the peak times based on the simulation of the circuit and the application of the DS PSD to

emulated pulses as well as deuterated stilbene pulses.

3.1. FDTF Optimization

We optimized the FDTF using the template pulses in Figure 2e as the input. Figure 9 shows the relative difference between neutron and gamma-ray PSD parameters for all 49 possible combinations of LG and HG peak times. The x-axis is the LG peaking time and the y-axis is the HG peaking time. Each small square is colored by the relative difference between the neutron and gamma-ray PSD parameter. The optimization showed that the difference between the LG and HG peaking times should be maximized in order to maximize the difference in PSD parameters. The combination that maximizes the difference between the LG and HG output values is 12.5 ns and 87.5 ns for the LG and HG peaking times, respectively. These optimized settings were used in the following experiments.

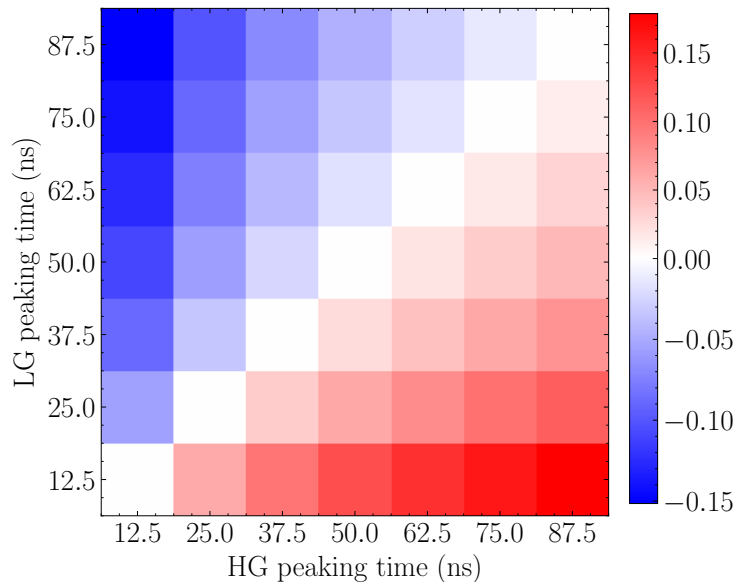


Figure 9: $\frac{PSD_n - PSD_\gamma}{PSD_\gamma}$ as a function of LG peaking time and HG peak time. The combination of 87.5 ns for the LG peaking time and 12.5 ns for the HG peaking time, produces the largest difference between the LG and HG PSD parameters than any other combination. This is shown by the colorbar labels as the darkest red is greater than 0.15 whereas the darkest blue is exactly -0.15.

3.2. Computational Results

With the optimized settings known, we can now test the performance of the DS PSD on dataset C, described in Section 2.4.1. The results of charge integration PSD, acquired using dataset B, and computational DS PSD results are shown in Figure 10 for comparison. Figure 10a shows the charge integration

result where the x-axis is the total pulse integral and the y-axis is the tail integral. Figure 10b shows the PSD obtained with the computational DS PSD method. The x-axis is the peak height of the LG signal and the y-axis is the peak height of the HG signal. We observed a good separation between the two groups of pulses, showing the feasibility of DS PSD on this dataset. Figure 12 shows the calculated FOMs for all the pulses shown in Figure 10, which range from 50 keVee to 1200 keVee.

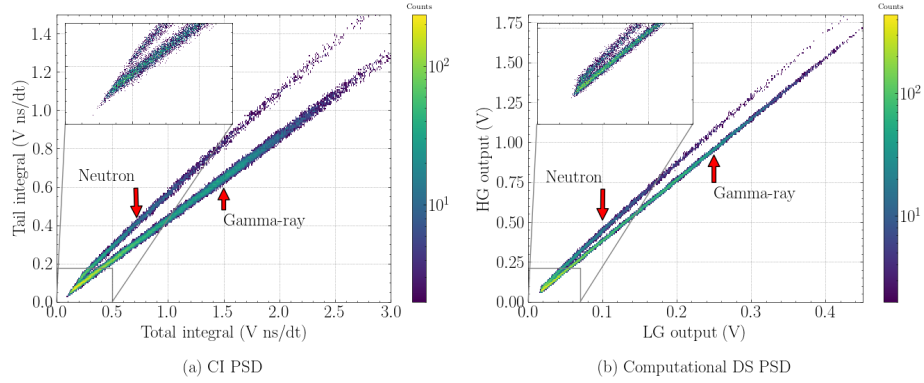


Figure 10: Comparison of (a) charge integration PSD and (b) computational DS PSD of the measured dataset acquired by measuring a PuBe with a stilbene-d₁₂ crystal.

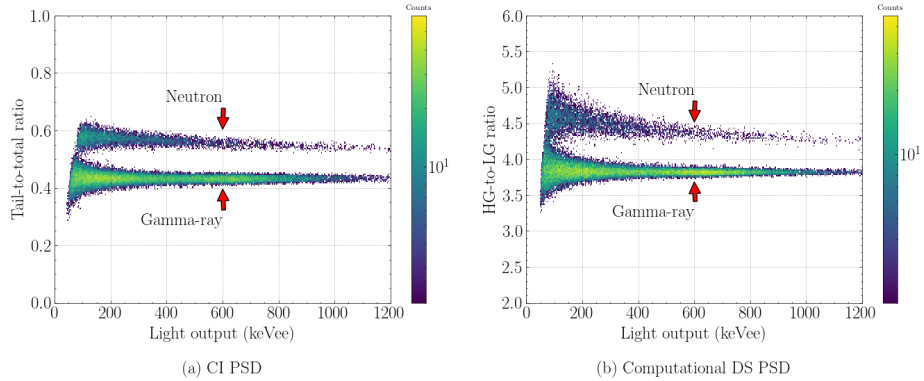


Figure 11: Comparison of (a) charge integration PSD and (b) computational DS PSD of the measured dataset acquired by measuring a PuBe with a stilbene-d₁₂ crystal.

3.3. Experimental Results

We used dataset A, described in Sec. 2.4.1, and input them to the A55CIT4-DT5550W system. We recorded the LG and HG output for each pulse and created a scatter plot of the LG output as a function of the HG output shown

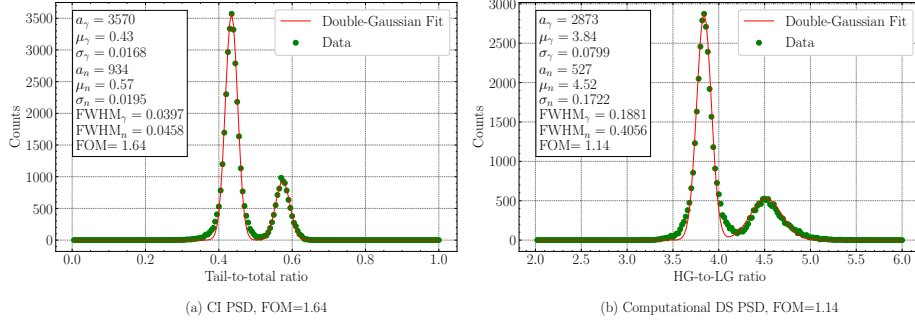


Figure 12: Comparison of the FOM for (a) charge integration PSD and (b) computational DS PSD of the measured dataset acquired by measuring a PuBe with a stilbene-d₁₂ crystal.

in Figure 13. Each color represents one pulse type with a different time constant. The x-axis and y-axis are the LG output and HG output in ADC units, respectively. The distinct separation shows that emulated pulses with different time constants yield a different PSD parameter and can be easily discriminated.

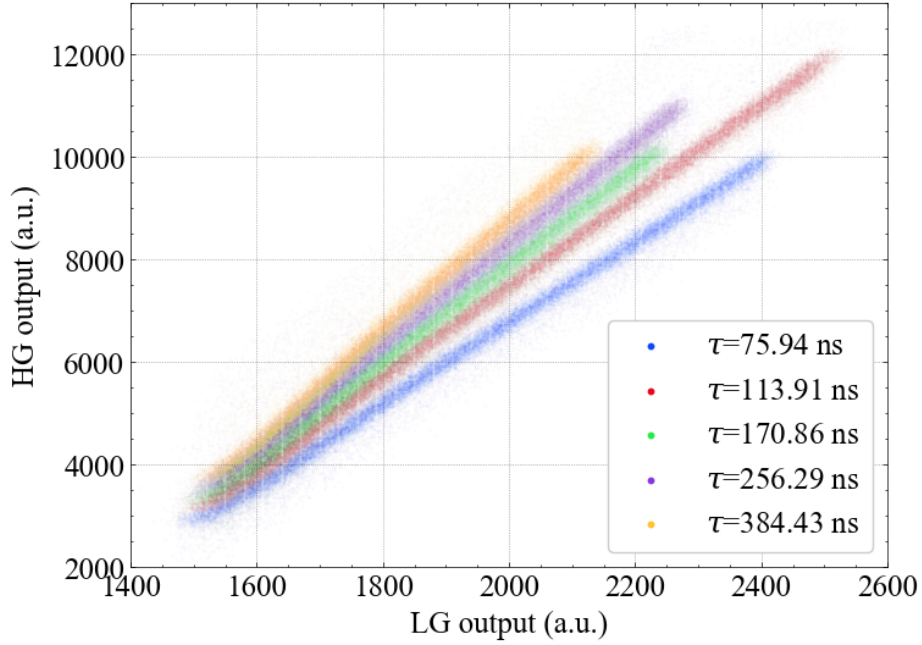


Figure 13: DS PSD of emulated pulses with different time constants.

The same analysis was performed on datasets B and C, described in Section 2.4.1. The results of charge integration PSD are shown in Figure 14a. The x-axis and y-axis are the total and tail integral, respectively. Figure 14b shows the

physical implementation of DS PSD. The x-axis and y-axis are the LG output and HG output, respectively. Separation between the neutron and gamma-ray bands is observed, indicating that DS PSD allows us to discriminate between neutrons and gamma rays. Using the method described in Section 2.4.2, we calculated the FOM for both the DS PSD and CI PSD methods, as shown by Figure 16. We also calculate the FOM for the first three light output bins for the CI and DS PSD methods and show the relationship between the PSD performance and light output in Figure 17. One can observe in Figure 17b (150-200 keVee) allows us to discriminate between gamma-ray and neutron pulses with minimum overlap between the two Gaussian distributions corresponding to these radiation types. The FOM of the DS PSD is smaller than that of the charge-integration.

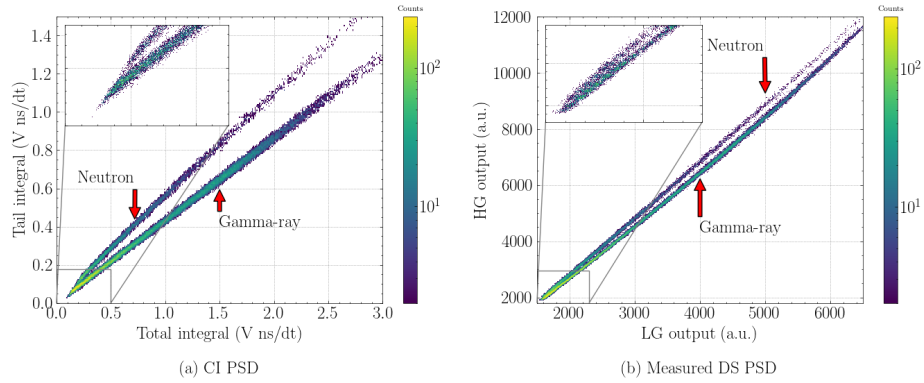


Figure 14: Comparison of (a) charge integration PSD and (b) DS PSD of deuterated stilbene pulses acquired by measuring a PuBe with a stilbene-d₁₂ crystal.

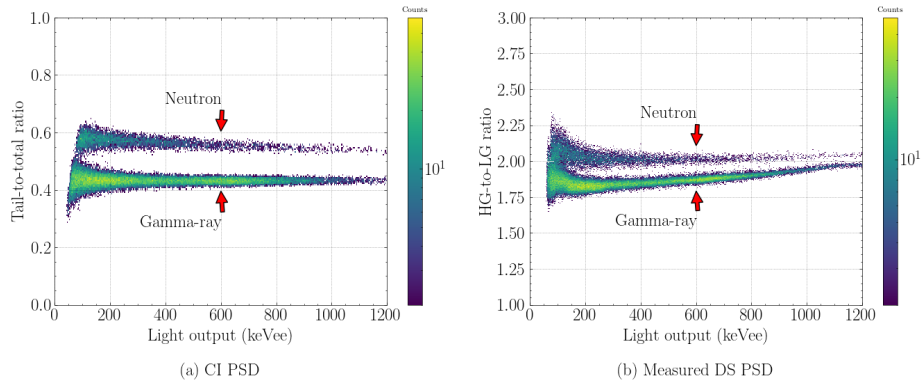


Figure 15: Comparison of (a) charge integration PSD and (b) DS PSD of deuterated stilbene pulses acquired by measuring a PuBe with a stilbene-d₁₂ crystal.

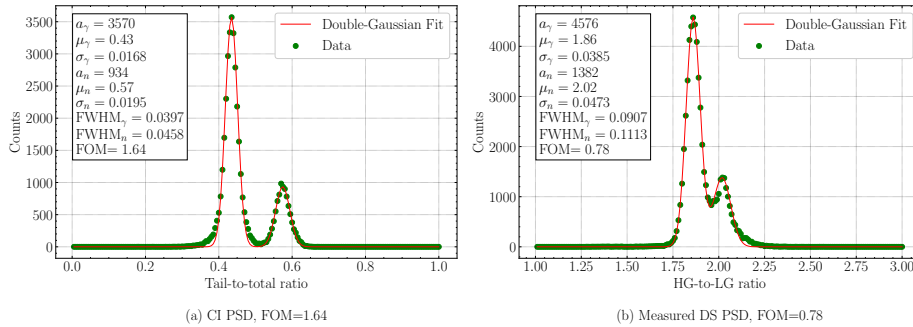


Figure 16: Comparison of the FOM for (a) charge integration PSD and (b) DS PSD acquired by measuring a $^{239}\text{PuBe}$ with a stilbene- d_{12} crystal.

4. Discussion and Conclusions

An on-board ASIC-based PSD method was developed on a commercially available platform, i.e., the Citiroc1A. This DS PSD method enables the discrimination of gamma-ray and neutron pulses within a light output range of 0.1 MeVee to 2 MeVee. The presented results show that the commercially available ASIC-based readout is capable of performing on-board PSD. Unlike the traditional CI method, we used the LG and HG paths intrinsic to the Citiroc1A to extract a shape-dependent PSD parameter, defined as the ratio between the output signal of the LG and HG paths. We developed an FDFT model to emulate the response of the shaping circuit in each path and then, using the FDFT model, we optimized the PSD parameter, i.e., the peak times of the LG and HG front end. The peak times that provided the best PSD parameter are 12.5-ns for the LG path and 87.5-ns for the HG path. The optimized PSD performance was estimated and compared to CI using a template-pulse data set. This study showed that the DS PSD performance is comparable to the current CI PSD. We then applied the DS PSD to synthetic pulses generated with a pulse emulator with controlled decay constants and confirmed experimentally that DS PSD can discriminate pulses of varying shapes. Finally, we applied the DS PSD to pulses acquired by measuring a $^{239}\text{PuBe}$ source with a deuterated stilbene crystal coupled to a SiPM. For this data set, the calculated FOM for DS PSD is 0.78 and 1.64 for CI PSD. Overall CI PSD outperforms DS PSD by 50%. Out of this 50%, about 30% can be attributed to the limited number of shaping times. This is shown by performing the computational analysis of DS PSD using the measured data set. The remaining observed decrease in FOM for the physical implementation of the DS PSD is likely due to noise on the low gain and high gain-shaped output signals, intrinsic to the ASIC itself. Although the DS PSD performance is worse than that of CI PSD, neutron and gamma-ray pulses can be effectively discriminated at light output values higher than 0.15 MeVee, corresponding to a neutron deposited energy of approximately 0.75 MeV. It should also be noted that DS PSD is performed on-board, in real time, and does not require the transfer of data to a separate system for further process-

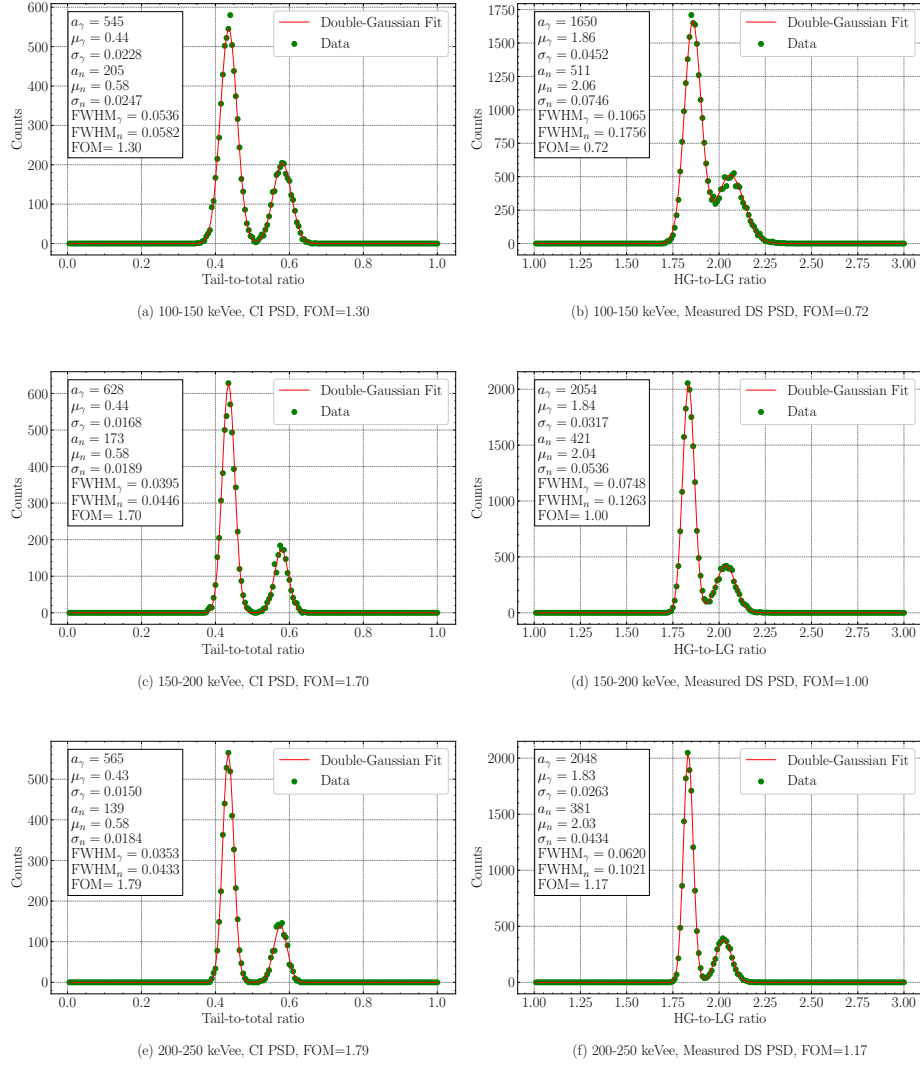


Figure 17: PSD performance in the first three light output bins.

ing. The Citiroc1A in this work has a total of seven available peak times. The DS PSD method could potentially be improved by finer tuning of the peak time, rather than selecting one of the seven options provided. We plan on testing the DS PSD performance using different organic scintillators, such as EJ-276D and small-molecule organic glass.

Acknowledgments

This material is based upon work supported by the Department of Energy National Nuclear Security Administration through the Nuclear Science and Security Consortium under Award Number DE-NA0003996.

References

- [1] J. E. M. Goldsmith, M. D. Gerling, J. S. Brennan, A compact neutron scatter camera for field deployment, *Review of Scientific Instruments* 87 (8) (2016) 083307. doi:10.1063/1.4961111.
- [2] P. F. Blosser, J. S. Legere, S. M. Dame, M. L. McConnell, U. Bravar, J. M. Ryan, A compton telescope for remote location and identification of radioactive material (2009) 302–307doi:10.1109/THS.2009.5168050.
- [3] J. E. M. Goldsmith, J. S. Brennan, M. D. Gerling, S. D. Kiff, N. Mascarenhas, J. L. Van De Vreugde, Miner - a mobile imager of neutrons for emergency responders (10 2014). doi:10.2172/1172910.
- [4] J. J. Manfredi, E. Adamek, J. A. Brown, E. Brubaker, B. Cabrera-Palmer, J. Cates, R. Dorrill, A. Druetzler, J. Elam, P. L. Feng, M. Folsom, A. Galindo-Tellez, B. L. Goldblum, P. Hausladen, N. Kaneshige, K. Keefe, T. A. Laplace, J. G. Learned, A. Mane, P. Marleau, J. Mattingly, M. Mishra, A. Moustafa, J. Nattress, K. Nishimura, J. Steele, M. Sweany, K. Weinfurther, K.-P. Ziock, The single-volume scatter camera, in: A. Burger, S. A. Payne, M. Fiederle (Eds.), *Hard X-Ray, Gamma-Ray, and Neutron Detector Physics XXII*, Vol. 11494, International Society for Optics and Photonics, SPIE, 2020, p. 114940V. doi:10.1117/12.2569995.
- [5] C. Piemonte, A. Gola, Overview on the main parameters and technology of modern silicon photomultipliers, *Nuclear Instruments and Methods in Physics Research Section A: Accelerators, Spectrometers, Detectors and Associated Equipment* 926 (2019) 2–15, silicon Photomultipliers: Technology, Characterisation and Applications. doi:10.1016/j.nima.2018.11.119.
- [6] L. Costrell, Development and current status of the standard nuclear instrument module (nim) system (1 1970). doi:10.2172/4059108.

- [7] N. Kornilov, V. Khriatchkov, M. Dunaev, A. Kagalenko, N. Semenova, V. Demenkov, A. Plompen, Neutron spectroscopy with fast waveform digitizer, *Nuclear Instruments and Methods in Physics Research Section A: Accelerators, Spectrometers, Detectors and Associated Equipment* 497 (2) (2003) 467–478. doi:10.1016/S0168-9002(02)01790-4.
- [8] CAEN, UM7028 A55CITx CITIROC Piggyback Board for DT5550W.
URL <https://www.caen.it/support-services/documentation-area/?documentbyname=A55CIT&type=all-categories>
- [9] CAEN, UM6697 DT5550W Weeroc ASICs evaluation and DAQ system.
URL <https://www.caen.it/products/dt5550w/>
- [10] S. Kinbara, T. Kumahara, A general purpose pulse shape discriminating circuit, *Nuclear Instruments and Methods* 70 (2) (1969) 173–182. doi:10.1016/0029-554X(69)90377-2.
- [11] L. Heistek, L. van der Zwan, Pulse shape discrimination with a comparator circuit, *Nuclear Instruments and Methods* 80 (2) (1970) 213–216. doi:10.1016/0029-554X(70)90764-0.
- [12] Weeroc, CITIROC1A Datasheet.
URL <https://www.weeroc.com/my-weeroc/download-center/citiroc-1a/89-citiroc1a-datasheet-v2-53/file>
- [13] Onsemi, Silicon Photomultipliers (SiPM), High PDE and Timing Resolution Sensors in a TSV Package J-Series SiPM Sensors.
URL <https://www.onsemi.com/pdf/datasheet/microj-series-d.pdf>
- [14] M. Morrocchi, G. Ambrosi, M. G. Bisogni, F. Bosi, M. Boretto, P. Cerello, M. Ionica, B. Liu, F. Pennazio, M. A. Piliero, et al., Depth of interaction determination in monolithic scintillator with double side sipm readout, *EJNMMI physics* 4 (2017) 1–25.
- [15] M. L. Ruch, P. Marleau, S. A. Pozzi, Position sensitivity within a bar of stilbene coupled to silicon photomultipliers, in: 2016 IEEE Nuclear Science Symposium, Medical Imaging Conference and Room-Temperature Semiconductor Detector Workshop (NSS/MIC/RTSD), IEEE, 2016, pp. 1–3.
- [16] CAEN, A7585D/DT5485P-PB Digital Controlled SiPM Power Supplies Rev.13.
URL <https://www.caen.it/products/a7585/>
- [17] J. Birks, D. Fry, L. Costrell, K. Kandiah, *The Theory and Practice of Scintillation Counting: International Series of Monographs in Electronics and Instrumentation*, International series of monographs on electronics and instrumentation, Elsevier Science, 2013.
URL <https://www.sciencedirect.com/book/9780080104720/the-theory-and-practice-of-scintillation-counting>

- [18] Y. Morishita, A. Di Fulvio, S. Clarke, K. Kearfott, S. Pozzi, Organic scintillator-based alpha/beta detector for radiological decontamination, Nuclear Instruments and Methods in Physics Research, Section A: Accelerators, Spectrometers, Detectors and Associated Equipment 935 (2019) 207–213. doi:10.1016/j.nima.2019.04.024.
- [19] J. Polack, M. Flaska, A. Enqvist, C. Sosa, C. Lawrence, S. Pozzi, An algorithm for charge-integration, pulse-shape discrimination and estimation of neutron/photon misclassification in organic scintillators, Nuclear Instruments and Methods in Physics Research Section A: Accelerators, Spectrometers, Detectors and Associated Equipment 795 (2015) 253–267. doi:10.1016/j.nima.2015.05.048.
- [20] CAEN, A5202/DT5202 64-Channel Citiroc-1A Unit for FERS-5200.
URL <https://www.caen.it/products/a5202/>
- [21] CAEN, UM5312 DT5810 Fast Digital Detector Emulator User Manual.
URL <https://www.caen.it/products/dt5810/>
- [22] W. G. J. Langeveld, M. J. King, J. Kwong, D. T. Wakeford, Pulse shape discrimination algorithms, figures of merit, and gamma-rejection for liquid and solid scintillators, IEEE Transactions on Nuclear Science 64 (7) (2017) 1801–1809. doi:10.1109/TNS.2017.2681654.